Ground layer correction: the heart of LINC-NIRVANA

Kalyan Kumar Radhakrishnan Santhakumari[a], Luca Marafatto[b,c], Maria Bergomi[b], Valentina Viotto[b], Jacopo Farinato[b], Roberto Ragazzoni[b], Tom Herbst[a], Thomas Bertram[a], Marco Dima[b], Peter Bizenberger[a], Florian Briegel[a], Frank Kittmann[a], Lars Mohr[a] and Demetrio Magrin[b].

[a]Max Planck Institut für Astronomie, Königstuhl 17, D-69117 Heidelberg, Germany;
[b]INAF - Osservatorio Astronomico di Padova, Vicolo dell'Osservatorio 5, I-35122 Padova, Italy;
[c]Università delgi Studi di Padova, Vicolo dell'Osservatorio 2, I-35122 Padova, Italy.

ABSTRACT

The delivered image quality of ground-based telescopes depends greatly on atmospheric turbulence. At every observatory, the majority of the turbulence (up to 60-80% of the total) occurs in the ground layer of the atmosphere, that is, the first few hundred meters above the telescope pupil. Correction of these perturbations can, therefore, greatly increase the quality of the image. We use Ground-layer Wavefront Sensors (GWSs) to sense the ground layer turbulence for the LINC-NIRVANA (LN) instrument, which is in its final integration phase before shipment to the Large Binocular Telescope (LBT) on Mt.Graham in Arizona.[19] LN is an infrared Fizeau interferometer, equipped with an advanced Multi-Conjugate Adaptive Optics (MCAO) module, capable of delivering images with a spatial resolution equivalent to that of a $\sim 23m$ diameter telescope. It exploits the Layer-Oriented, Multiple Field of View, MCAO approach[3] and uses only natural guide stars for the correction. The GWS has more than 100 degrees of freedom. There are opto-mechanical complexities at the level of subsystems, the GWS as a whole, and at the interface with the telescope. Also, there is a very stringent requirement on the superposition of the pupils on the detector. All these conditions make the alignment of the GWS very demanding and crucial. In this paper, we discuss the alignment and integration of the left-eye GWS of LN and detail the various tests done in the lab at INAF-Padova to verify proper system operation and performance.

Keywords: LBT, LINC-NIRAVANA, GLAO, star enlarger, ground layer correction, MCAO

1. INTRODUCTION

In order to deliver high quality images to the beam combiner for interferometry, LINC-NIRVANA[1] (LBT INterferometric Camera - Near-InfraRed / Visible Adaptive iNterferometer for Astronomy), called LN here after, uses Multiple Field of View (MFoV) Layer-Oriented (LO) Multi-Conjugate Adaptive Optics[2–4] (MCAO) using only Natural Guide Stars (NGSs) for the correction. This is realized using *pyramid* wavefront sensing.[5] LN uses two different Field of Views (FoVs) to correct for two different turbulent layers above the telescope pupil.

The prominent turbulent layer is the ground layer, up to $100m$ above the telescope pupil. Aberrations caused in this layer will be corrected by Ground layer Wavefront Sensors (GWSs), using the light received from up to 12 stars in an annular $2'$-$6'$ FoV. The GWS drives the Adaptive Secondary Mirror (ASM, 672 actuators) of the Large Binocular Telescope[6] (LBT). *Higher layer* aberrations will be corrected by Mid-High Wavefront Sensors (MHWSs), conjugated to $7.1km$ above the telescope pupil, using the light received from up to 8 stars in the inner $2'$ FoV. The MHWS output controls the Xinetics deformable mirror (349 actuators) located on the LN bench. The scientific FoV of the LN instrument is the innermost $10''$x$10''$.

Light from the scientific object is received by both primary mirrors. After reflection from the ASMs and the tertiary mirrors, it enters the LN bench which has identical components for the light coming from both the primary mirrors. (The right side is called DX and the left side SX). There are, therefore, 2 GWSs and 2 MHWSs. The correction is done in the visible wavelength regime. A *dichroic* mirror splits the beam from the inner $2'$ FoV into visible and Near-InfraRed (NIR). The visible part continues to the MHWS while the NIR part is directed

Send correspondence to *kalyan@mpia.de*

Adaptive Optics Systems IV, edited by Enrico Marchetti, Laird M. Close, Jean-Pierre Véran, Proc. of SPIE Vol. 9148, 91482R · © 2014 SPIE
CCC code: 0277-786X/14/$18 · doi: 10.1117/12.2054988

to the scientific camera, where the beams from both SX and DX interfere and the fringes are produced. From the fringes, the image is reconstructed.[7,8]

In the following sections, we describe the GWS, its sub-systems, the precision requirements as well as the alignment data and various performance test results. Also, the current status of the GWS systems are mentioned.

2. THE GROUND LAYER WAVEFRONT SENSOR

The incoming $F/15$ beam is intercepted by an annular mirror which reflects the $2'$-$6'$ annular FoV towards the GWS while the inner $2'$ FoV part continues. The GWS is optically conjugated to the ground layer. According to the estimated slopes of the wavefront measured by the GWS, corresponding signals are sent to the ASM of the respective arm with a maximum frequency of $1KHz$. The ASMs are equipped with 672 voice-coil force actuators which will correct perturbations introduced by the ground layer. GWS is composed of 3 main units. (1) Star Enlargers (SEs), (2) The Pupil Re-Imager (PRI) unit and (3) the main mechanical structure.

The light of 12 NGSs in the annular FoV continues inside the GWS toward 12 optical devices, called *star enlargers*. The implementation of the LO technique poses some technical difficulties, due to the large size of the re-imaged pupils produced on the detector by the *pyramids*. This would require using large optics with fast focal ratio and large CCDs. Large CCDs have long readout times, which are not compatible with the correction time scales for typical adaptive optics systems. The size of the pupils can be reduced by increasing the focal ratio F of the incident beam on the tip of the pyramid. This is done using star enlargers,[9] which locally increase the focal ratio of the light from the NGS while maintaining the separations between the NGSs. In this way, the rest of the field of view retains the focal ratio F, while the guide stars get magnified according to the new focal ratio F'. The magnification factor of the SE is $k = F'/F$. The SEs are mounted on mechanical arms placed on the motorized stages (figure 1). This allows for movement of the SEs across the field to acquire their respective guide stars.

The light from each pyramid is then optically superimposed. Since the GWS is conjugated to the ground layer, the pupils produced from each of the SEs must perfectly superimpose on the detector. This is accomplished by the *pupil re-imager*,[10] which consists of an annular flat mirror, a parabolic mirror and an objective. The annular flat mirror reflects the beams received from the SEs to the parabolic mirror which converges them towards the objective, a system of 4 custom achromatic doublets, located in the central hole of the flat mirror (figure 2). The beams coming out of the PRI are captured by a Marconi Applied Technologies CCD50 EEV with 128x128 pixels. The optical superposition of the signals, typical of the LO method, allows fainter reference stars, as long as their integrated magnitude is greater than the typical pyramid WFS limiting magnitude.

The optical components are integrated into the main mechanical structure. It consists of three main components - a cylindrical structure supporting the star enlargers, a bearing which allows the system to rotate, and a support structure of carbon fiber which attaches the GWS to the LN bench. The mechanical structure secures the GWS, provides rigid support for the SEs and the PRI, and allows the cabling of all the electronics. The de-rotating mechanics compensates for sky rotation, thereby preventing the images of the NGSs from going out of the FoV of the corresponding SE.[11] The GWS after the integration of the sub-systems and just before shipping to MPIA can be seen in figure 7.

To quantify the known errors, such as uncertainties in the manufacture of components, errors due to misalignment of individual components etc., an *error budget* has been created.[12] The errors are evaluated as the *blur of the* 4 *re-imaged pupils*. A pupil is divided into sub-apertures. The blur results in the relative displacement of the sub-apertures of the different pupils. This means that there will be a cross-talk at the superposition from the light of different pupils. To minimize this effect, the shift (blur) must be smaller than the sub-aperture size. In our case, the minimum sub-aperture is $48\mu m$. Errors always accumulate. It is therefore necessary to check each and every sub-component of the system and every possible phenomenon which could introduce blur. For example, better alignment of the SE optics produces better the superposition of the 4 pupils created by each pyramid. The pupil blur can be converted into a WaveFront Error (WFE).[10] The overall WFE results allow us to estimate the achievable Strehl Ratio (SR). The result of the error budget computation is that the SR in the J and K bands is 0.71 and 0.89 respectively. Considering the requirements, the GWS-SX had been aligned.

GWS-SX alignment was completed at INAF, Padova in October 2013 and the sensor was shipped to MPIA, Heidelberg, where it presently awaits the flexure tests to be done on the LN bench. In the following sections, we present the different alignment data and results right from the sub-system level to the GWS internal alignment as a whole. Several tests were performed after the internal alignment of the system to check its performance. These tests are also described along with the outcomes.

3. GWS-SX INTERNAL ALIGNMENT

Experience from the alignment of the GWS-DX made the alignment of GWS-SX relatively faster.

In particular, in the GWS-DX alignment, it was discovered that some lenses were sliding inside their barrels during the bearing rotation. This resulted in the necessity to glue the lenses inside their mounts and to restart the alignment from the beginning, causing a substantial loss of time.[11] For the GWS-SX, all the lenses were glued before aligning the SEs internally.

GWS-SX alignment[13] proceeded in the following way:

- Internal alignment of the 12 SEs,
- Internal alignment of the PRI,
- Integration of the sub-systems to the main mechanical structure and
- GWS-SX internal alignment.

Finally, several performance tests were carried out, and when all were successful, the alignment was declared complete.

3.1 SE internal alignment

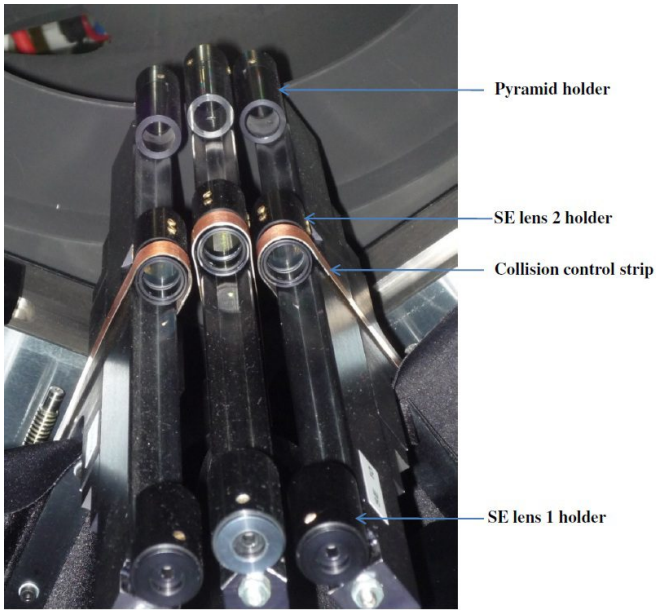

Figure 1. Three star enlargers mounted in the GWS-SX. Collision control strips are used to protect the star enlargers from collision as there is overlap of the regions spanned by the neighboring SEs. When the collision control strips come in contact, the movement of those SEs are frozen.

The SE increase the focal ratio of the incident beam from $F/15$ to $F/187.5$ on the pin of the pyramid, thereby enlarging the image of the star. A single tar enlarger contains 3 optical components - two achromatic doublet

lenses and a refracting pyramid. The barrels holding these optical components can be seen in figure 1. The lenses must be centered and aligned properly in tip-tilt so that the star image falls on the pin of the pyramid with the same magnification factor, k, for each of the SEs. The value of $k = 12.5$ with the RMS repeatability smaller than 1/240 is the requirement. The deviation from this value would violate the error budget and the pupil radii between different SEs and would result in improper superposition on the detector and higher the wavefront error. The magnification factors of all SEs appear in table 1. The mean resulting value is $k = 12.50$ and the measured RMS repeatability is 1/570, far lower than 1/240. The requirement is fulfilled.

SE#	**k**	**SE#**	**k**	**SE#**	**k**
SE1	12.50	SE5	12.53	SE9	12.53
SE2	12.50	SE6	12.47	SE10	12.51
SE3	12.51	SE7	12.51	SE11	12.49
SE4	12.50	SE8	12.50	SE12	12.55

Table 1. The measured magnification factors for the GWS-SX SEs.

3.2 PRI internal alignment

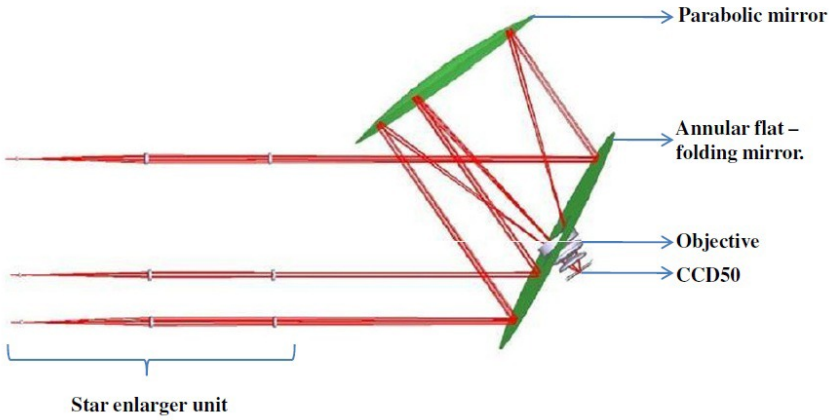

Figure 2. The pupil re-imager optical design. The red lines show the light path from the LBT focus passing through the star enlargers and PRI reaching the CCD50 detector.

The PRI re-images and superimposes the 4 pupils generated by each of the 12 SEs on the detector (see figure 2). The PRI has a focal ratio of $F/0.9$. The optical quality of the images on the detector depends directly on the optical quality of the PRI. Therefore, proper centering, tip-tilt and focus of the parabolic mirror and the objective are very crucial and demanding. The optical quality of the PRI is measured in terms of the RMS spot radius of re-imaged point source on the detector for on-axis and off-axis positions. The requirement is to achieve centrally symmetric optical quality with an RMS spot radius less than $13\mu m$ across the 0.44° radius FoV. The PRI internal alignment procedure sets the parabolic mirror and the objective in their ideal nominal position. For performing the alignment, we used a test CCD with 2560x1920 pixels each $2.2\mu m$ size. This allows higher spatial sampling and therefore better precision in the alignment than does the final CCD50, which has 128x128 pixels each $24\mu m$ size. The alignment of the PRI is done in different phases.[10,13] To qualitatively verify the coma aberration symmetry, we took spot images in and out of focus position at the boundaries of the FoV (0.44° radius). The outcome appears in figure 3. Each spot is defocused by a fixed amount from its "best focus position".

The RMS spot radius is computed for each image, considering only the pixel values over a threshold of 5%

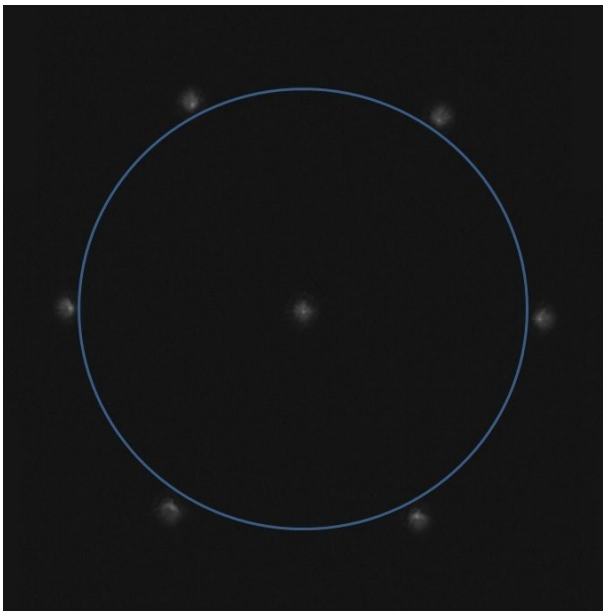

Figure 3. Spot images taken in an out-of-focus position at 0.44° radius FoV, qualitatively verifying the coma aberration symmetry.

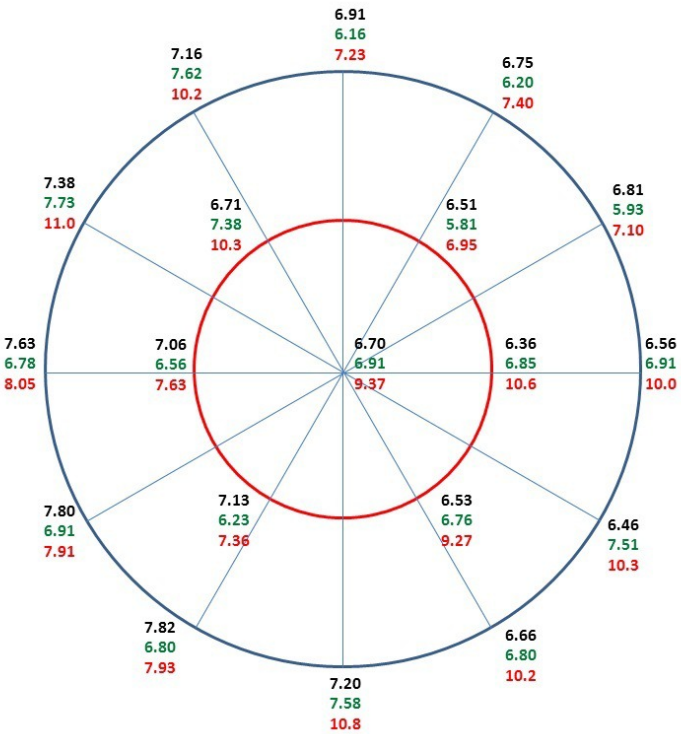

Figure 4. PRI Optical Quality Check - Spot radius measurements for different positions along the PRI FoV. The blue and the red circles represent the 0.44° and 0.22° radius FoVs. Black values are the results of a Gaussian fit to the spot, while green and red values are the measured RMS spot radii considering only the pixel values over a threshold of 10% and 5% of the peak intensity of the spot respectively. All values are in μm.

and 10% of the peak intensity of the spot at the center of the FoV. Moreover, a Gaussian fitting is also computed. The results appear in figure 4.

All of the RMS spot radii of the sampled spots are lower than $13.0\mu m$. The requirement is, therefore, fulfilled.

3.3 Integrating the sub-systems and final alignment

As the first step, the PRI is integrated into the mechanical structure and is aligned to the bearing rotation axis using its flat folding mirror. This sets the center of the PRI FoV coincident to the bearing rotation axis. The optical quality is checked again for different positions in the FoV and for 120° rotation of the bearing. The outcome appears in figure 5. The RMS spot radius is always found to be less than $13\mu m$.

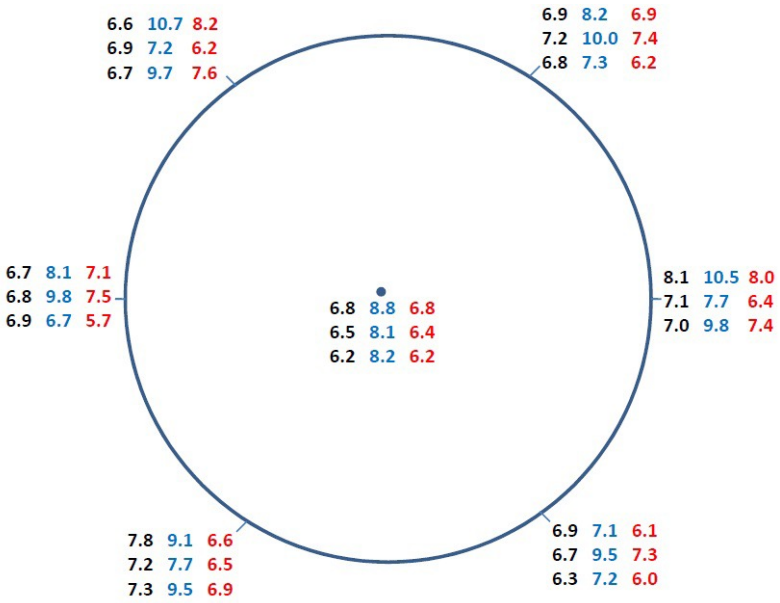

Figure 5. The optical quality after alignment of the flat mirror of the PRI. The first, second and third rows represent +60°, 0° and −60° rotation of the bearing. As in figure 4, black values represent the Gaussian fit radius of the spot while blue and red values are the measured RMS spot radii considering only the pixel values over a threshold of 5% and 10%, respectively, of the peak intensity of the spot. All values are in μm.

The SEs are then integrated on the linear stages using a T-shaped mechanical interface. The relative alignment of the SEs is very important to avoiding bad pupil superposition on the detector. Both the relative tip-tilt and differential pyramid rotation will result in a relative shift of the pupils produced by the SEs and consequently imperfect superposition, leading to errors in the wavefront reconstruction and to a loss of delivered Strehl ratio. The requirements appear in the table 2.

Item	**Measured effect**	**Requirement**
SE tip-tilt	Four spots shift with respect to goal position	$4.8\mu m$ (5″ SE tilt)
Pyramid rotation	Four spots rotation	$10\mu m$
SE defocus	Defocus signal	$20nm$ WFE

Table 2. Star enlarger alignment requirements during its integration to GWS.

The SEs have to not only be aligned in tip-tilt and pyramid rotation angle, but also they must be properly positioned in focus with respect to the $F/15$ incident beam with a precision requirement of $100\mu m$, corresponding to a WFE of $20nm$. The LBT focal plane is spherical. There is therefore a large difference in the focal plane

position along the optical axis, depending on the distance from the center of the field (see figure 6). The pyramids we use for wavefront sensing are non-modulated. Therefore, care has been taken to ensure that the enlargement of the spots due to the defocus term is smaller than the "equivalent seeing" at the pin of the pyramid. Otherwise, the defocus term will saturate the pyramid WFS and retrieval of the higher order aberrations becomes impossible. The LBT focal plane appears in figure 6. The actual peak to valley of the focal plane in the GWS is $4.94mm$, translating to the condition that the seeing must be worse than $0.55''$. Statistics provided by Large Binocular Camera at LBT show that the median seeing is $\sim 1''$. There will therefore certainly be observing time with seeing less than $0.5''$. To make sure that defocus term does not saturate the pyramid WFS, the SEs are split into two groups - odd SEs and even SEs. The first group spans the $1'$-$2.2'$ radius area and the second one the $2.2'$-$3'$ radius area, in a way that the two regions have equal areas and have a similar residual defocus WFE at the edges. The odd SEs are aligned and focused to a radius of $1.71'$, and their offset is $1.93mm$ from the on-axis focus position, while the even SEs are aligned to a radius of $2.63'$, with an offset of $4.5mm$. The maximum residual defocus for both groups with respect to the LBT focal surface is $1.37mm$. The seeing must therefore be better than $0.15''$ to become an issue, which is a rather unlikely and rare case. If, however, there is a common defocus or any other static aberration on the detector, it can be subtracted during the calibration procedure.

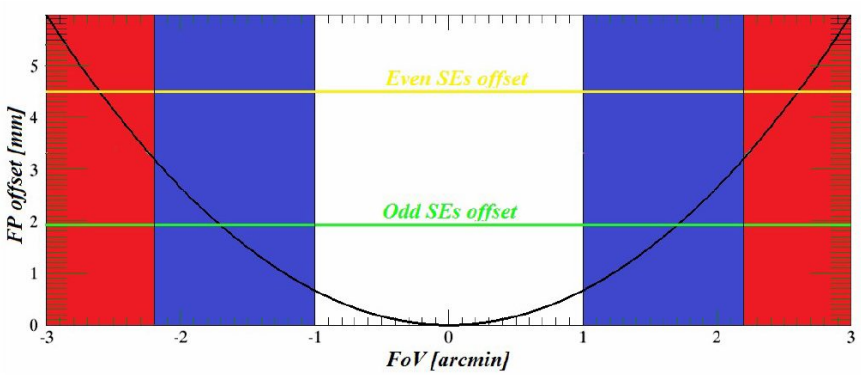

Figure 6. Curvature of the LBT focal plane for a $6'$ FoV. The *colored* areas show the $2'$-$6'$ diameter annular FoV which is re-imaged at the GWS entrance focal plane. The *blue* area is the FoV covered by the odd-SEs, focused on an offset represented by the *green* line. The *red* area is the FoV covered by the even-SEs, focused on an offset represented by the *yellow* line. The two offsets have been chosen to minimize the residual defocus WFE in their respective regions.

Comparing the measured values in table 3 with the requirements listed in table 2, the alignment results are inside tolerances for the respective items. The SEs alignment requirements are therefore fulfilled. The GWS-SX is internally aligned (see figure 7).

4. PERFORMANCE TESTS

In order to check the reliability of GWS-SX during various situations and to verify that the pupil blur values included in the error budget were not underestimated, performance tests were conducted. The tests and their outcomes are described below.

4.1 Pupil stability during bearing rotation

GWS-SX has been aligned internally in a static configuration. At the telescope, the bearing will rotate to compensate for sky rotation. As the bearing rotates, the gravity vector changes. This could lead to flexure, misalignment, and consequently, pupil blur. The presence of 12 SEs, each consisting of 3 optical components and the fact that each SE can move in a wide annular FoV and send the light to the common PRI, makes the system opto-mechanically complex. The necessity of very good superposition of the pupils at the CCD while capturing the images makes it further complex. Hence, the bearing rotation invariably introduces difficulty in pupil superposition stability. A test was therefore performed to check the pupil superposition stability during rotation. To analyze the differential movement between the SEs, images of 4 spots from each of the SEs were

SE #	**SE tip-tilt**[μm]	**Pyramid rotation**[$arcmin$]	**SE defocus**[nm WFE]
SE01	2.7	0.1	4.3
SE02	1.6	-0.2	1.9
SE03	3.3	0.9	-2.3
SE04	2.3	0.6	0.2
SE05	3.1	-1.3	8.9
SE06	1.7	-0.5	-7.4
SE07	0.9	1.8	0.4
SE08	1.7	1.2	2.6
SE09	2.6	-0.7	-5.3
SE10	2.2	-0.9	2.6
SE11	1.8	0.7	1.3
SE12	2.4	-0.1	-7.3

Table 3. Star enlarger alignment results after integration in the GWS-SX.

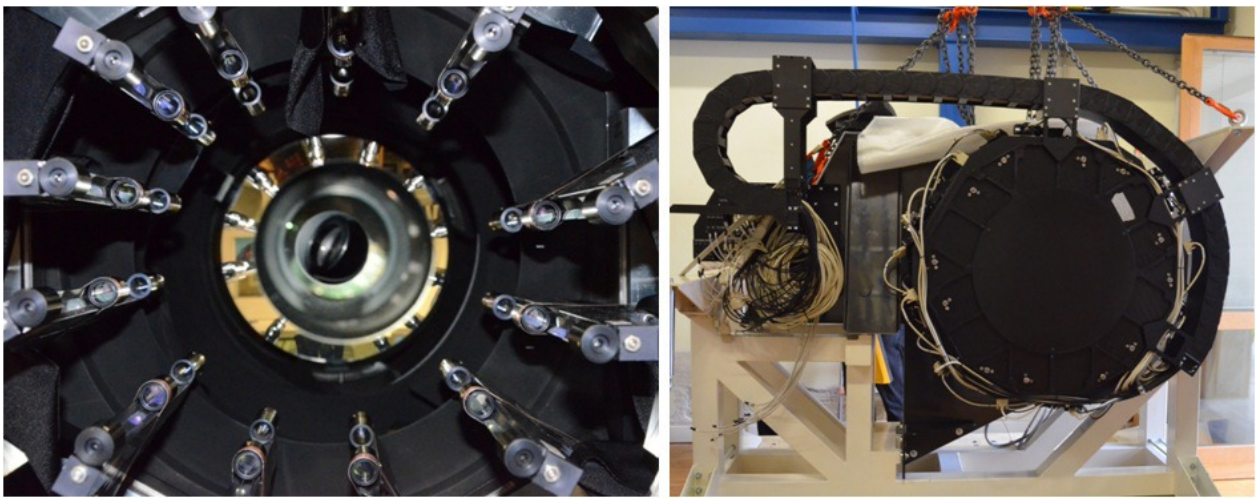

Figure 7. *Left* - The GWS-SX during its internal alignment. The 12 mounted SEs, the PRI, and the objective are visible. *Right* - GWS-SX ready for shipment from INAF-Padova to MPIA.

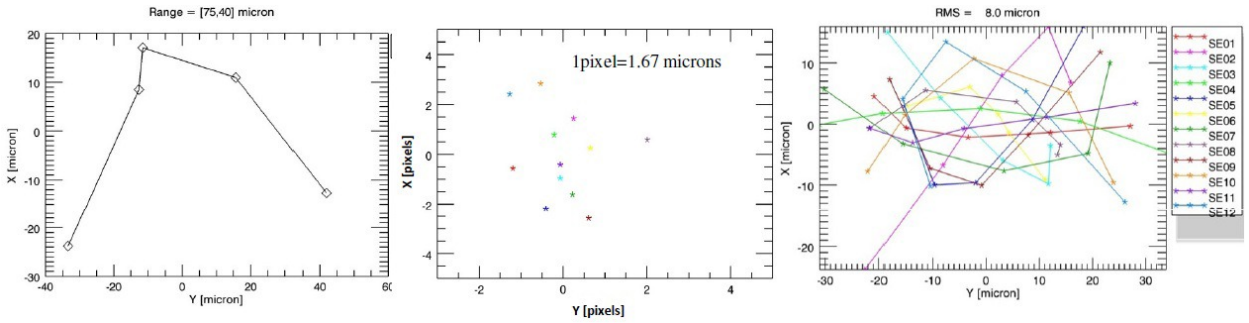

Figure 8. The pupil movements on the test CCD for a complete 120° rotation of the GWS-SX. The plot on the left shows the common mode, common to all the SEs. The middle plot indicates the relative positions that the barycenters of the 4 spots produced by each SE should have when the bearing is at 0° to minimize the RMS differential movements. The plot on the right represents the differential movement of the SEs.

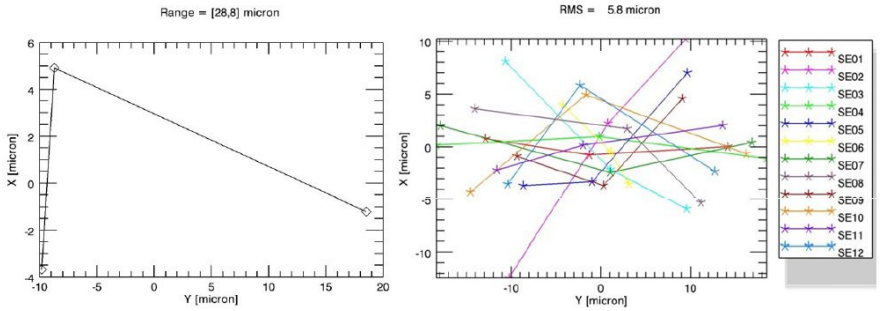

Figure 9. The pupils movement for the best 60° rotation of the GWS-SX. The plot on the left shows the common mode while the right figure shows the differential movement of the SEs.

taken at 5 different positions of the bearing; +60°, +30°, 0°, −30°, −60°. Visually, the spots moved back and forth. Over plotting the curves obtained for each SE for both directions, we observed the same behavior.

After a complete bearing rotation, we analyzed the barycenter of the 4 spots produced by each SE at the five bearing positions to measure their shift. The GWS performance was affected by both bearing wobble and PRI & CCD flexure. This was common to all SEs and for this reason, we call it the *common mode*. The common mode can be estimated and removed with software. In reality, it will be removed by moving the CCD to counter-act the effect of all sources which contribute to the common mode. For GWS-DX, the common mode had a higher value than for SX. Since there is a large contribution by the CCD mount, a new CCD case for the GWS-SX has been designed, which is lighter to reduce flexure. It is also smaller to allow safer mobility of the CCD which must move very close to the flat mirror of the PRI and the objective. In addition, the new case is equipped with pre-loading mechanism to further diminish its flexure and consequently the common mode.

When the common mode is subtracted, we get *differential movement* of the SEs. The RMS value of pupil movement decreased from $75\mu m$ to $8\mu m$ after removal of the common mode for 120° of rotation (see the left and right plots on figure 8). This value is within the requirement of $11.1\mu m$. Fine tuning is performed for each of the SEs to further minimize the RMS differential movement on the complete rotation (middle plot of figure 8), thereby increasing the pupil superposition stability.

Despite its capability to perform a 120° rotation, the system is required to rotate for a maximum of 60° during one observation, due to fringes rotation in the interferometric focal plane. For the best 60° rotation range (−30° to +30°), the RMS blur due to the differential movement of the SEs was found to be $5.8\mu m$ (see figure 9). The pupil blur due to bearing rotation is well within the requirement.

4.2 Pupil blur for SE linear movements

This test measures the shift of each SE 4-pupil matrix on the detector when the SE moves in its travel range. The shift has been measured by illuminating the SEs with a monochromatic collimated beam and computing the movement of the 4 spots re-imaged on the CCD during the movement of the SE along a predefined path. The SEs trajectories appear in the figure 10 and are considered representative of the SE behavior in its operational range.

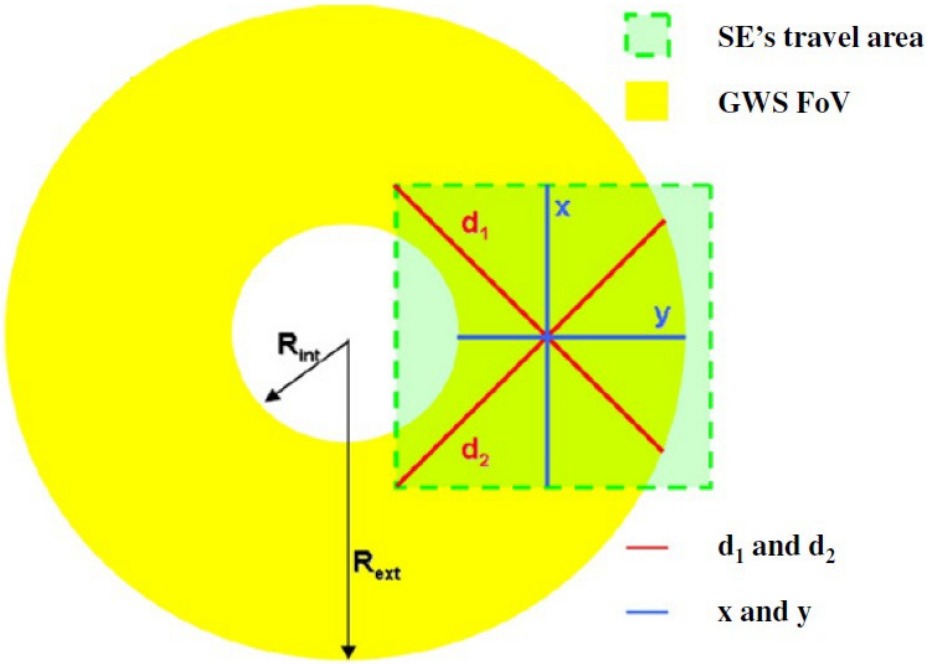

Figure 10. The travel range of a star enlarger. The yellow region is the GWS FoV, the green region shows the SE's travel area. The blue lines represent the x- and y-axis of the SE movements. The movement along the orthogonal red line trajectories with distances d_1 and d_2 are used to estimate the blur caused due its linear movements.

The shift is the result of the following sources: (1) linear stage wobble, (2) PRI optical quality, (3) SE tilt due to ring flexure (a small fraction and hence neglected) and (4) SE tilt due to stage flexure (a small fraction and hence neglected). The movement of the SE support does change slightly the torque applied to the linear stage, and correspondingly to the rings supporting them. However, the weight of the SE is very small in comparison to a single linear stage, so we neglect this effect. The requirement derived from the error budget is a pupil blur due to this contribution less than $13.9\mu m$.

The $13.9\mu m$ value is compatible with most of the measured RMS blurs. The results appear in table 4. The measured blurs for SE04 and SE09 are higher than this value, even in the y-operational range. However, the range which will be actually spanned by the SEs is even smaller, because of the split of the FoV into two annuli as mentioned in section 3.3. If the corresponding ranges are considered, the measured wobble is reduced below $13.9\mu m$ for all the SEs. The requirement is therefore fulfilled.

4.3 Pupil image cosmetics

This test checks if there are some unwanted but relevant features in any of the re-imaged pupils. The images of 4 pupils re-imaged from each of the 12 SEs are shown in figure 11. The small bumps visible at the edge of the pupils are due to the mount of one of the setup lenses. The black dots are due to the diffraction of dust on the test camera CCD. The pupils are homogeneously illuminated. The cosmetics are fine.

SE #	**x**[μm]	**y-whole range**[μm]	**y-operational range**[μm]
SE01	2.5	5.4	2.9
SE02	1.7	5.4	5.4
SE03	4.2	4.2	2.9
SE04	4.6	33.7	14.2
SE05	4.2	10.0	9.2
SE06	1.7	7.1	6.2
SE07	6.7	11.8	6.2
SE08	2.5	5.4	3.3
SE09	2.5	27.5	17.5
SE10	2.5	35.0	8.4
SE11	1.7	10.0	4.6
SE12	3.3	3.3	2.9

Table 4. Test results of SE linear stage wobble for GWS-SX. The "y-operational range" value is the actual range inside which the SEs explore the 2 to 6 *arcmin* FoV.

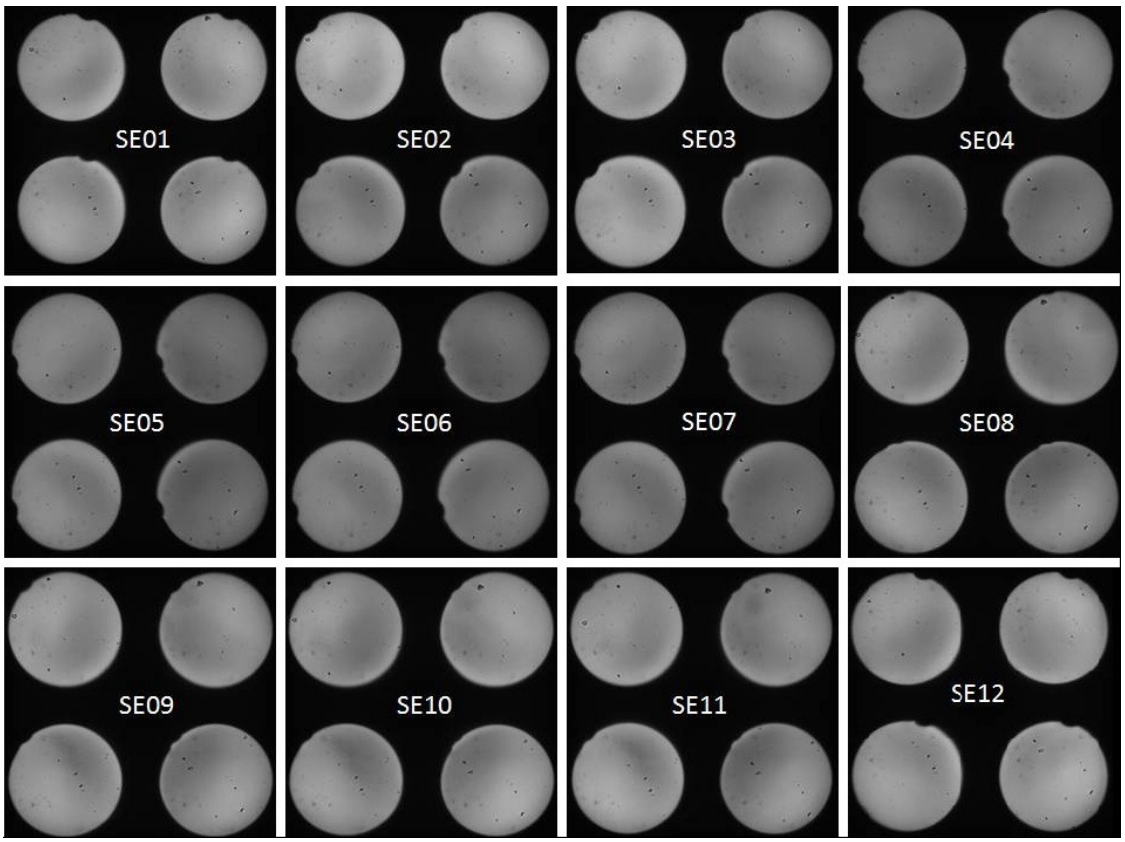

Figure 11. The pupil cosmetics of the GWS-SX SEs.

4.4 Throughput of GWS-SX

The throughput measures the transmittance of each of the aligned SEs and hence the relative transmittance with respect to the average value. The total throughput of the GWS-SX is also evaluated. An $F/15$ white beam is focused onto each of the SEs. Using a photo-diode, the input power and the output power of the beam are measured just in front of the SE and just coming out of the SE respectively. The throughput for each of SEs is computed. The average throughput is 87% with the relative transmittance of SEs with respect to the average within $\pm 3\%$. The transmittance of the mirrors coating is $92\%(@633nm)$ and that of the objective is $93.5\%(@633nm)$. Therefore the total throughput is 74%. The requirement is 62%. The throughput is well within the requirement.

5. STATUS

GWS-DX was aligned[12] at INAF-Padova during 2011-12 and underwent flexure tests[14] at MPIA, Heidelberg during early 2012. It was shipped to LBT in early 2013 as part of the Pathfinder experiment.[14–16]

GWS-SX is currently at MPIA, Heidelberg. The flexure tests on GWS-SX will be performed at the LN bench soon. CCD50 tests are also ongoing. Simultaneously, some final electronics checks are running, such as working of the motors for the bearing rotation.

The updates regarding other LN sub-systems are also presented in this conference.[17–19]

6. CONCLUSIONS

Ground layer turbulence accounts for up to $60\% - 80\%$ of the total aberration of the incoming wavefront. Therefore, a very good ground layer correction is essential for MCAO and interferometric imaging. This makes the ground layer wavefront sensors very much the heart of LINC-NIRVANA. More than 100 degrees of freedom, complex opto-mechanics, stringent requirements on the pupil superposition stability during static and rotating configurations etc. make the alignment of the GWS a very demanding and critical task. In this paper, we have discussed the details of the internal alignment of the GWS-SX. It passed all of the tests to confirm system performance, such as checking the optical quality of the system, pupil superposition stability in different configurations, pupil cosmetics etc. These tests verified that all optical components are fixed to their mounts and none of them make any unwanted jumps during bearing rotation. This was initially an issue for GWS-DX. Flexure tests, which will happen soon at MPIA after mounting GWS-SX to the LN bench, will again confirm this. We will then have a fully working ground layer wavefront sensor for both the DX and SX arms. The GWS-SX will be shipped to LBT, along with the LN bench and its other sub-systems, in early 2015.

ACKNOWLEDGMENTS

KKRS acknowledges the support and motivation from the AstroMundus consortium throughout the duration of this work. He also extends his gratitude to the people of INAF-Padova for the warm hospitality they provided.

REFERENCES

[1] Herbst T.M., Ragazzoni R., Andersen D. , Bhnhardt H., Bizenberger P., Eckart A., Gaessler W., Rix H.W., Rohloff R.R., Salinari P., Soci R., Straubmeier C., Xu W., *"LINC-NIRVANA, a Fizeau beam combiner for the Large Binocular Telescope,"* Proc. SPIE 4838, 456-465 (2003).

[2] Beckers J.M., *Detailed compensation of atmospheric seeing using multiconjugate adaptive optics*, Proc.SPIE 1114, 215-217 (1989).

[3] Ragazzoni R., Diolaiti E., Farinato J., Fedrigo E., Marchetti E., Tordi M., Kirkman D., *"Multiple Field of View Layer Oriented Adaptive Optics. Nearly whole sky coverage on 8 m class telescopes and beyond,"* A&A 396, 731 (2002).

[4] Farinato J., Ragazzoni J., Arcidiacono C., Brunelli A., Dima M., Gentile G., Viotto V., Diolaiti E., Foppiani I., Lombini M., Schreiber L., Bitzenberger P., De Bonis F., Egner S., Gssler W., Herbst T.M., Krster M., Mohr L., Rohloff R.R., *"The Multiple Field of View Layer Oriented wavefront sensing system of LINC-NIRVANA: two arcminutes of corrected field using solely Natural Guide Stars,"* Proc. SPIE 7015 (2008).

[5] Ragazzoni R., *"Pupil plane wave front sensing with an oscillating prism,"* J. Mod. Opt. 43, 289-293 (1996).
[6] Hill J. M., Salinari P., *"Large Binocular Telescope Project,"* Proc. SPIE 4004, 3646 (2000).
[7] Correia S., Carbillet M., Boccacci P., Bertero M., Fini L., *"Restoration of interferometric images. I. The software package AIRY,"* A&A 387, 733743 (2002).
[8] Carbillet M., Correia S., Boccacci P., Bertero M., *"Restoration of interferometric images. II. The case-study of the Large Binocular Telescope,"* A&A 387, 744757 (2002).
[9] Ragazzoni R., Diolaiti E., Vernet E., Farinato J., Marchetti E., Arcidiacono C., *"Arbitrarily Small Pupils in Layer-Oriented Multi-Conjugate Adaptive Optics,"* ASP 187, 860 (2005).
[10] Viotto V., *"From 8(m) To 8(mm): Wavefront Sensing From Cosmological to Human Scales,"* PhD Thesis, Università delgi Studi di Padova, January 2012.
[11] Viotto V., Bergomi M., Mohr L., *"LINC-NIRVANA-Ground-layer Wavefront Sensor Design Report,"* LN-INAFP-DES-AO-001-0.3, INAF Padova, October 2013.
[12] Marafatto L., Bergomi M., Brunelli A., Dima M., Farinato J., Farisato G., Lessio L., Magrin D., Ragazzoni R., Viotto V., Bertram T., Bizenberger P., Brangierc M., Briegel F., Conrad A., DeBonis F., Herbst T., Hofferbert R., Kittmann F., Krster M., Meschke D., Mohr L., Rohloff R.R., *"Aligning a more than 100 degrees of freedom wavefront sensor,"* Proc. SPIE 8447, 84476F-1 (2012).
[13] Radhakrishnan Santhakumari K.K., *"Removal of the ground layer for the very large telescopes,"* Master's Thesis, Università delgi Studi di Padova, September 2013.
[14] Bergomi M., Viotto V., Farinato J., Marafatto L., Radhakrishnan K., Ragazzoni R., Dima M., Magrin D., Arcidiacono C., Diolaiti, E., Foppiani I., Lombini M., Schreiber L., Bertram T., Bizenberger P., Conrad A., Herbst T., Kittmann F., Kopon D., Meschke D., Zhang X., *"Multiple FoV MCAO on its way to the sky,"* Proc. AO4ELT Conference, Florence, May 2013.
[15] Bergomi M., Viotto V., Arcidiacono C., Baumeister H., Bertram T., Berwein J., Briegel F.,Conrad A.R., Farinato J., Herbst T., Hofferbert R., Kopon D., Kittmann F., Marafatto L., Ragazzoni R., *"First light of the LINC-NIRVANA Pathfinder experiment,"* This conference, June 2014.
[16] Kopon D., Conrad A.R., Bertram T., Herbst T., Berwein J.,Ragazzoni R., Farinato J., Viotto V., Bergomi M., Marafatto L., Kittmann F., Rohloff R-R., Baumeister H., De Bonis F., Hofferbert R., Arcidiacono C., Puglisi A.T., Brunelli A., Pott J-U., Bizenberger P., Briegel F., Krster M., Mechke D., Mohr L., Zhang X., *"Pathfinder first light: alignment, calibration, and commissioning of the LINC- NIRVANA ground-layer adaptive optics subsystem,"* This conference, June 2014.
[17] Moreno-Ventas J., Baumeister H., Bertram T., Bizenberger P., Briegel F., De Bonis F., Herbst T., Mohr L., Kittmann F., Radhakrishnan K., *"Optical integration and verification of LINC-NIRVANA,"* This conference, June 2014.
[18] Bizenberger P., Baumeister H., Herbst T., Laun W., Mohr L,Moreno-Ventas J. *"LINC-NIRVANA: Diffraction limited optics in cryogenic environment,"* This conference, June 2014.
[19] Herbst T., Ragazzoni R., Eckart A., Weigelt G.P., *"The LINC-NIRVANA Fizeau interferometric imager: final lab integration, First Light experiments and challenges"* This conference, June 2014.